

Modeling RIS from Electromagnetic Principles to Communication Systems—Part II: System-Level Simulation, Ray Tracing, and Measurement

Le Hao, *Member, IEEE*, Sravan K. R. Vuyyuru, *Member, IEEE*, Sergei A. Tretyakov, *Fellow, IEEE*, Artan Salihu, *Graduate Student Member, IEEE*, Markus Rupp, *Fellow, IEEE*, and Risto Valkonen, *Member, IEEE*

Abstract—In this paper, we systematically study the electromagnetic (EM) and communication aspects of a RIS through EM simulations, system-level and ray tracing simulations, and finally measurements. We simulate a nearly perfect, lossless RIS, and a realistic lossy anomalous reflector (AR) in a ray tracer and analyze the large-scale fading of simple RIS-assisted links. We also compare the results with continuous and quantized unit cell reflection phases with one to four-bit resolutions. Finally, we perform over-the-air communication link measurements in an indoor setting with a manufactured sample of a wide-angle AR. The EM, system-level, and ray tracing simulation results show good agreement with the measurement results. It is proved that the introduced macroscopic model of a RIS from the EM aspects is consistent with our proposed communication models, both for an ideal RIS and a realistic AR. The verified system-level simulator and ray tracer for a RIS could be tailored to, e.g., the wireless communication system engineers in the cellular network planning business, providing tools to optimize network performance.

Index Terms—Anomalous reflector, reconfigurable intelligent surface (RIS), system-level simulator, ray tracing, 6G.

I. INTRODUCTION

RECONFIGURABLE Intelligent Surfaces (RIS) have attracted considerable attention in recent years. This technique is considered as an emerging technology for the next generation of wireless communications due to its potential to improve coverage and energy efficiency in wireless networks [1]. Unlike conventional reflectors or antennas, a RIS comprises multiple unit cells capable of dynamically altering their electromagnetic properties for different incoming waves. For example, by tuning the phase shifts of each unit cell, the RIS can actively control, redirect, and enhance electromagnetic

This work was supported in part by the European Union's Horizon 2020 MSCA-ITN-METAWIRELESS project, under the Marie Skłodowska-Curie grant agreement No 956256, and in part by the Vienna Science and Technology Fund (WWTF) [Grant ID: 10.47379/VRG23002]. (*Corresponding author: Le Hao*)

Le Hao, Artan Salihu, and Markus Rupp are with the Institute of Telecommunications, Technische Universität Wien (TU Wien), 1040 Vienna, Austria. Artan Salihu is also with the Christian Doppler Laboratory for Digital Twin assisted AI for sustainable Radio Access Networks, Austria. (e-mail: le.hao@tuwien.ac.at; artan.salihu@tuwien.ac.at; markus.rupp@tuwien.ac.at).

Sravan K. R. Vuyyuru is with Nokia Bell Labs, 02610 Espoo, Finland, and also with the Department of Electronics and Nanoengineering, School of Electrical Engineering, Aalto University, 02150 Espoo, Finland (e-mail: sravan.vuyyuru@aalto.fi).

Sergei A. Tretyakov is with the Department of Electronics and Nanoengineering, School of Electrical Engineering, Aalto University, 02150 Espoo, Finland (e-mail: sergei.tretyakov@aalto.fi).

Risto Valkonen is with Nokia Bell Labs, 02610 Espoo, Finland (e-mail: risto.valkonen@nokia-bell-labs.com).

waves in desired directions [2]. This can, as a result, improve the system performance, e.g., more or stronger propagation paths for higher throughput, lower latency, higher reliability, higher energy efficiency, etc. [3]. RIS technology can also be used for sensing and localization, security enhancement, and interference cancellation, etc. [4].

To make the best use of the RIS technology and realize it in the real world, the electromagnetic (EM) properties and communication performance of RISs in realistic scenarios have to be investigated. The EM perspective of the RIS-related research has been addressed in Part I of this paper, including RIS design, EM simulation, and optimization problems. With the designed RIS from Part I of this research, we focus on its communication aspects in this part, including different path loss models for RIS-assisted links, ray tracing and system-level simulations, and communication link measurements.

Recent studies have focused on studying path-loss modeling in RIS-assisted wireless networks [5]–[17], as summarized in Table I for ease of reference. To the best of the authors' knowledge, there are no works on this paper's topic. Even though a broad range of RIS-related research activities have been done in recent years, there is still a lack of a systematic study of RIS from the EM design to communication models. The models from the literature are based on the notion of the local reflection coefficient from different points of the RIS panels, but this field model is not necessarily efficient or even electromagnetically consistent, and in practice, it is not possible to independently control the response of each individual array element. In addition, there are no works on analyzing a realistic RIS in a ray tracer or in a system-level simulator. It is essential to build connections between the theory and practice, as well as between the EM design part and the communication analysis part.

To fill the gap, in this work, we systematically study the communication link performance of a RIS that is designed based on the EM theory of array scattering synthesis methodology [18], [19]. The key contributions of this paper are summarized as follows: (i) We define the appropriate controllable parameters of RIS panels and next analyze the large-scale fading of the designed RIS through the *Vienna SLS* and with EM simulation results. (ii) We integrate the designed RIS into a ray tracer to compare the ray tracing simulation results with the theoretical outcomes. (iii) We execute measurements using a manufactured AR prototype and compare the experimental results with theoretical analysis and ray tracing simulations. To

TABLE I
LIST OF REPRESENTATIVE PAPERS RELATED TO CHANNEL MODELS INCLUDING RIS

Reference	Main contributions
[5], [6]	Demonstrate the scaling law governing the power reflected from a RIS is influenced by various factors, such as the RIS size and the mutual distances between the RIS and the transmitter/receiver with measurements.
[7]	Overview of RIS-based channel measurements and experiments, large-scale path loss models, and small-scale multipath fading channel models, as well as channel characterization issues of RIS-assisted wireless communication systems.
[8]	Introduce a macroscopic model for evaluating the multi-mode re-radiation and diffuse scattering from a RIS, which can be integrated with ray-based models such as ray tracing and ray launching for realistic radio propagation simulations.
[9]	Introduce a macroscopic model for metasurface scattering at the beginning or at the end of the interaction chain and perform ray tracing simulations in an indoor scenario for a lossy, phase-gradient anomalous reflector (AR).
[10], [11]	Introduce the RIS-tailored Vienna system-level simulator (SLS) [12] with a <i>MATLAB</i> ray tracer interface, including different path loss models for system-level simulations.
[13]	Evaluate the system performance of a RIS-assisted cellular network through system-level simulations, such as the outdoor and indoor coverage and ergodic rate with different-sized RISs and under different frequency bands.
[14]	Present key propagation-related characteristics and optimal phase shift solutions of RISs and perform ray tracing simulations of RISs in indoor and outdoor scenarios at 28 GHz.
[15]	Use a commercial ray tracing tool, <i>Wireless Insite</i> [16], to capture the propagation characteristics of RISs, and formulate a non-convex optimization problem that minimizes the number of RISs under rate constraints.
[17]	Present a uniform ray description of electromagnetic wave scattering by locally periodic metasurfaces of polygonal shape, and extend the ray-based models to large environments outfitted with metasurface panels.

the best knowledge of the authors, this is the first work that systematically studies a RIS from the EM design to the system-level and ray tracing simulations, then to model validation by prototype manufacturing and link measurements. This is also the first work on implementing a perfectly designed RIS and a realistic lossy AR to a ray tracer with the performance verified through theory.

The remainder of this paper is organized as follows. Section II introduces two methods of large-scale fading analysis and compares the results. Section III explains the RIS modeling in a ray tracer and compares the ray tracing simulation with theoretical results. In Section IV, we present experimental results for the manufactured panel and compare them with ray tracing simulations. Finally, conclusions and outlook are drawn in Section V.

II. LARGE-SCALE FADING ANALYSIS

In this section, we first introduce two theoretical models of large-scale fading in RIS-assisted links. At this stage, we assume a far-field propagation scenario with a single line-of-sight (LOS)-path communication link. One of the studied methods is based on a theoretical estimation of the response of perfectly functioning ARs [20], which means that the parasitic scattering into specular directions and all other possible propagating Floquet harmonics is completely suppressed. This method has been incorporated in the Vienna SLS and is denoted as Method 1. The other method is based on EM-simulated RIS directivity patterns, and we name it Method 2. Next, the differences between these two models are compared to investigate whether the EM simulation results are consistent with the theoretical analysis for such a RIS. In addition, we analyze the quantization effect of the RIS from the large-scale fading point of view.

A. Method 1

A recently published path loss model [20], derived from an approximate electromagnetic solution for scattered fields from a RIS, has been implemented in the Vienna SLS. This model

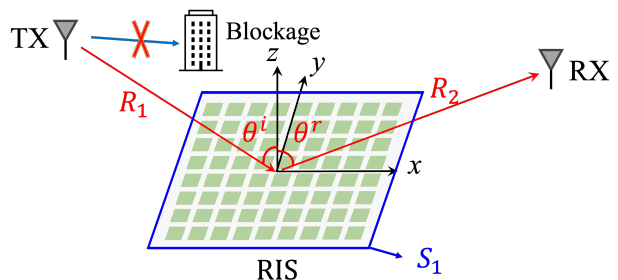


Fig. 1. An illustration of the TX-RIS-RX link with the LOS path between the TX and RX is blocked.

is designed only for far-field propagation scenarios, and it is not applicable to near-field cases. Therefore, in this paper, we only analyze the far-field performance of RISs, and the near-field analysis is postponed to our future work. With this path loss model, the received power at the RX antenna is calculated as

$$P_r = P_t G_t(\theta_t, \phi_t) G_r(\theta_r, \phi_r) \eta_{\text{eff}} \left(\frac{S_1}{4\pi R_1 R_2} \right)^2 |\cos \theta^i \cos \theta^r|, \quad (1)$$

where $0 < \eta_{\text{eff}} \leq 1$ is the RIS efficiency parameter that takes into account parasitic absorption in a RIS as well as design and manufacturing imperfections. An estimation of η_{eff} for phase-gradient reflectors can be found in Fig. 2 in [21]. That estimation is based on the mismatch of the characteristic impedances of the incident and reflected plane-wave modes that cannot be eliminated using the phase-gradient design method. More advanced design methods, such as e.g. in [18], allow realizations of scanning anomalous reflectors with efficiencies close to 100%. S_1 is the geometrical area of the RIS panel. The parameters θ^i and θ^r represent the incidence and reflection angles at the position of the RIS, respectively. The transmit power is indicated as P_t , while $G_t(\theta_t, \phi_t)$ and $G_r(\theta_r, \phi_r)$ represent the gains of the TX and RX antennas, respectively. θ_t , ϕ_t , θ_r , and ϕ_r represent the elevation angle and the azimuth angle from the TX antenna to the RIS, and the

elevation angle and the azimuth angle from the RX antenna to the RIS, respectively. The distance between the base station (TX) and the RIS is denoted by R_1 , while the distance between the RIS and the user (RX) is denoted by R_2 . An illustration of the application scenario and the parameters of this model are shown in Fig. 1.

B. Method 2

Another path loss model for a RIS-assisted link is based on the notion of RIS directivity and gain. The directivity is defined in terms of the electric field far-field pattern $F(\theta, \phi)$ as [22]:

$$D(\theta, \phi) = \frac{4\pi F(\theta, \phi)}{\int_0^{2\pi} \int_0^\pi F(\theta, \phi) \sin \theta d\theta d\phi}, \quad (2)$$

where $F(\theta, \phi)$ is the far-zone radiation intensity pattern. The gain is calculated as

$$G(\theta, \phi) = e_{cd} D(\theta, \phi), \quad (3)$$

where e_{cd} is the panel efficiency. If RIS losses can be neglected, we have $e_{cd} = 1$.

In this work, we consider the designed RIS from Part I and calculate its gain numerically, using *CST* software. That is, we obtain the radiation pattern of the RIS $F(\theta, \phi)$ from *CST* simulations and then use Eq. (2) and Eq. (3) to calculate the RIS gain values. We calculate the gain values for four different RIS states (i.e., four different reflection angles) each for five different sizes of RIS panels. The RIS gain results for the continuous load impedance design are listed in Table II. It is worth noting that each RIS model needs two gain values: G_{rx} is the RIS gain in the direction from RIS to TX, and G_{tx} is the RIS gain in the direction from RIS to RX. Since the RIS that we use here is designed for the normal incidence angle and four reflection angles, i.e., 13° , 27° , 43° , and 65° , we only calculate G_{rx} value at 0° , and G_{tx} values at the four reflection angles. From Table II we observe that G_{rx} values are larger than G_{tx} , that is because the incidence angle is 0° and G_{rx} values are also at 0° which reflect the most energy due to specular reflection, but G_{tx} values are further away from 0° and thus the gain values are also reduced. From Table II in the first part of this paper, we also know that the optimized RIS reflection efficiencies from RIS state 1 to state 4 (named “Mode 1” to “Mode 4” in Part I) are 99.6, 99.3, 99.5, and 99.1 for continuous loads. When the reflection angle is further away from the normal direction, the lower reflection efficiency also results in lower RIS gain values.

Once we obtain the RIS gains from *CST* simulations, the received power at the RX antenna through the RIS can be calculated according to Friis’ formula for the links between TX and RIS and then between RIS and RX [22]:

$$P_1 = G_t(\theta_t, \phi_t) G_{rx}(\theta_{rx}, \phi_{rx}) \left(\frac{\lambda}{4\pi R_1} \right)^2, \quad (4)$$

$$P_2 = G_{tx}(\theta_{tx}, \phi_{tx}) G_r(\theta_r, \phi_r) \left(\frac{\lambda}{4\pi R_2} \right)^2, \quad (5)$$

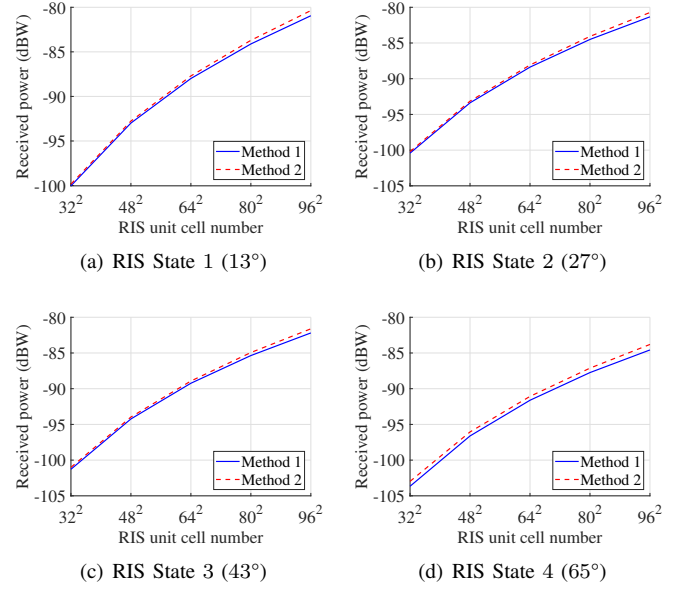


Fig. 2. Results comparison between methods 1 and 2 with 5 different RIS sizes.

which gives the following path loss estimation [23]:

$$P_r = P_t P_1 P_2 = \frac{P_t G_t(\theta_t, \phi_t) G_{rx}(\theta_{rx}, \phi_{rx}) G_{tx}(\theta_{tx}, \phi_{tx}) G_r(\theta_r, \phi_r) \lambda^4}{(4\pi)^4 (R_1 R_2)^2}. \quad (6)$$

Here, θ_{tx} , ϕ_{tx} , θ_{rx} , and ϕ_{rx} represent the spherical angles defined from the RIS to the TX antenna, and from the RIS to the RX antenna, respectively. This equation is equivalent to the path loss model derived from the radar range equation in [24].

C. Comparison Between the Analytical Path Loss Model and Simulations

Here, we compare the path loss estimations obtained using both methods for a simple case of a single beyond LOS link TX–RIS–RX containing two LOS sub-channels. As an example, we set $G_t = G_r = 1$, $R_1 = 17$ m and $R_2 = 17.22$ m, $\eta_{eff} = 1$. According to the design parameters of the RIS, the working angles are $\theta^i = 0^\circ$ and $\theta^r = 13^\circ, 27^\circ, 43^\circ, 65^\circ$ for RIS states 1 to 4, respectively. The test RIS areas are $S_1 = 32 \times 32 A_0$, $48 \times 48 A_0$, $64 \times 64 A_0$, $80 \times 80 A_0$, and $96 \times 96 A_0$ where $A_0 = (1.1034\lambda/4)^2$ is the area of one unit cell. The common parameters in Eq. (6) are set the same as Eq. (1). G_{rx} and G_{tx} in Eq. (6) are the computed values from Table II with continuous loads. The results of the received power from the two methods are shown in Figs. 2(a), 2(b), 2(c), and 2(d) for RIS states 1 to 4, respectively.

From Fig. 2 we can observe that for all four RIS states, the two methods give very close results. The differences between the two methods are about 0.2 dB to 0.6 dB for RIS state 1, state 2, and state 3 when the RIS sizes change from $32 \times 32 A_0$ to $96 \times 96 A_0$. For state 4 the difference is from 0.7 dB to 0.8 dB with the five sizes.

This agreement is expected because Eq. (1) is valid for theoretically perfect ARs, and from Part I we saw that the

TABLE II
DIFFERENT-SIZE RIS GAINS FOR CONTINUOUS AND QUANTIZED LOADS

RIS State	Resolution	$32 \times 32 A_0$		$48 \times 48 A_0$		$64 \times 64 A_0$		$80 \times 80 A_0$		$96 \times 96 A_0$	
		G_{tx} (dB)	G_{rx} (dB)								
State 1 (13°)	Continuous	29.86	30.04	33.36	33.61	35.84	36.19	37.76	38.27	39.33	40.04
	4 bit	29.86	30.03	33.35	33.61	35.84	36.19	37.76	38.26	39.32	40.03
	3 bit	29.78	29.95	33.28	33.52	35.76	36.10	37.68	38.18	39.26	39.95
	2 bit	29.57	29.73	33.06	33.30	35.54	35.88	37.47	37.95	39.04	39.70
	1 bit	27.20	27.28	30.69	30.81	33.17	33.34	35.10	35.35	36.68	37.02
State 2 (27°)	Continuous	29.49	30.04	32.99	33.61	35.47	36.19	37.39	38.27	38.97	40.04
	4 bit	29.45	30.01	32.95	33.58	35.43	36.16	37.36	38.23	38.93	40.00
	3 bit	29.45	29.99	32.94	33.56	35.42	36.14	37.35	38.22	38.93	39.98
	2 bit	29.23	29.76	32.71	33.33	35.20	35.90	37.12	37.97	38.70	39.72
	1 bit	26.46	27.03	29.94	30.53	32.42	33.04	34.35	35.02	35.94	36.68
State 3 (43°)	Continuous	28.69	30.03	32.16	33.61	34.63	36.19	36.54	38.26	38.09	40.03
	4 bit	28.51	29.87	31.99	33.44	34.45	36.01	36.36	38.09	37.92	39.84
	3 bit	28.51	29.86	31.98	33.43	34.45	36.01	36.36	38.08	37.93	39.84
	2 bit	28.37	29.68	31.82	33.24	34.28	35.81	36.19	37.87	37.74	39.62
	1 bit	24.97	26.37	28.46	29.88	30.94	32.39	32.87	34.38	34.44	36.03
State 4 (65°)	Continuous	26.72	30.04	30.07	33.61	32.47	36.19	34.35	38.27	35.90	40.04
	4 bit	26.65	30.00	30.01	33.57	32.41	36.15	34.29	38.22	35.84	39.98
	3 bit	26.16	29.56	29.52	33.11	31.93	35.67	33.81	37.72	35.36	39.46
	2 bit	25.97	29.36	29.32	32.90	31.73	35.45	33.61	37.50	35.17	39.22
	1 bit	22.31	25.89	25.70	29.34	28.13	31.81	30.06	33.77	31.65	35.40

RIS design with continuous loads gives a nearly perfect performance. In fact, it can be shown that for ideal ARs with continuous current distribution the considered two path loss models are equivalent. The model of Eq. (1) assumes that the RIS captures all the power that is incident on its surface and retransmits it without imperfections. This means that if we consider the same RIS as a conjugate-matched receiving antenna, its effective area A_{eff} is equal to the geometrical area of the panel cross-section, that is, $A_{\text{eff}} = S_1 |\cos \theta^i|$. Likewise, in the transmit regime, we have $A_{\text{eff}} = S_1 |\cos \theta^r|$. Using the general relation between the effective area and gain, valid for any linear and reciprocal antenna,

$$G = 4\pi \frac{A_{\text{eff}}}{\lambda^2}, \quad (7)$$

We can find the RIS gains for an ideal AR in terms of the panel area and the incidence and reflection angles:

$$G_{\text{rx}} = 4\pi \frac{S_1}{\lambda^2} |\cos \theta^i| \quad (8)$$

and

$$G_{\text{tx}} = 4\pi \frac{S_1}{\lambda^2} |\cos \theta^r|. \quad (9)$$

The product of the two gains of the RIS panel is related to its bi-static scattering cross section σ as

$$G_{\text{rx}} G_{\text{tx}} = \frac{4\pi}{\lambda^2} \sigma, \quad (10)$$

and this a function of both angles of incidence and observation. Substituting Eq. (8) and (9) into Eq. (6) we obtain the same equation as Eq. (1). Therefore, these two methods are equivalent if the RIS operates perfectly. The small differences between the two methods are from the RIS gain differences given by Eqs. (8) and (9), and they result from the spatial discretization of the reflecting surface.

From [11] we conclude that when the RIS size is doubled, the received power should achieve 6 dB gain for a tuned RIS. In these four figures, the received power has about 7.0 dB,

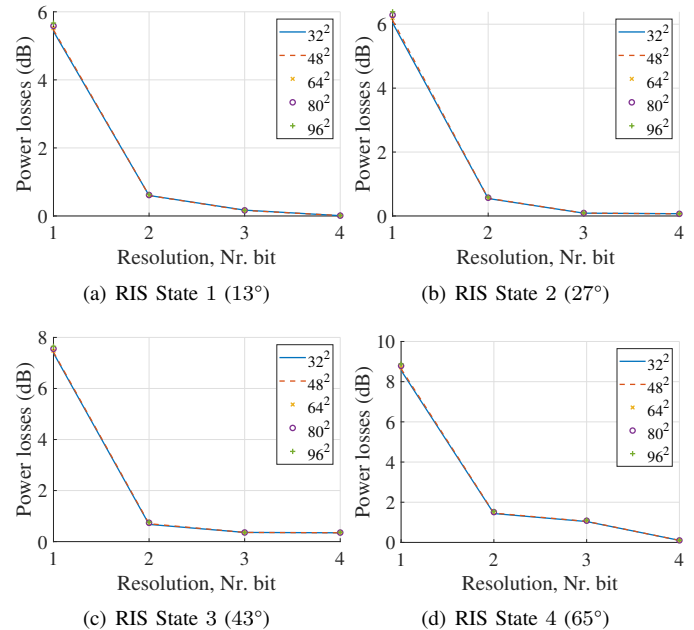


Fig. 3. Power loss of load-quantized RISs for different sizes.

5.0 dB, 3.9 dB and 3.2 dB differences for the RIS sizes $32 \times 32 A_0$ to $48 \times 48 A_0$, from $48 \times 48 A_0$ to $64 \times 64 A_0$, from $64 \times 64 A_0$ to $80 \times 80 A_0$, and from $80 \times 80 A_0$ to $96 \times 96 A_0$, respectively. Since the RIS size $64 \times 64 A_0$ is four times larger than the size $32 \times 32 A_0$, the received power with $64 \times 64 A_0$ size is 12.0 dB higher than for the $32 \times 32 A_0$ -sized RIS, which can also be found in Table II. Similarly, the difference between $48 \times 48 A_0$ and $96 \times 96 A_0$ -sized RIS is 12.1 dB, which is consistent with the power scaling law [25].

D. Load Quantization Analysis

The RIS gain values used in Sec. II-C are from the optimization of continuous reactive loads, corresponding to the assumption that the controllable loads can have arbitrary reactive impedances. In this section, we use the RIS gain results obtained from quantized load impedances, which are

summarized in Table II, to investigate the difference between different quantization resolutions. From Part I we explained that the reflection efficiency of the RIS increases when the load quantization resolution changes from 1-bit to 4-bit. This is because the unit cell loads optimization results become more efficient when we have more load impedance values (2 values for 1-bit and 16 values for 4-bit). The reflection wave is more concentrated in the desired directions and the side lobes are better suppressed, which is why the RIS gain values in the desired directions also become higher and gradually get close to the gain when using continuous loads.

In Fig. 3 we compare the received powers between the designs based on continuous and quantized load values. Figures 3(a), 3(b), 3(c), and 3(d) show the results for RIS states 1, 2, 3, 4, respectively. The differences between the panels of 5 different sizes are almost the same for all four RIS states. As expected, when the resolution increases from 1-bit to 4-bit, the differences between the continuous loads designs and the discrete loads become smaller for all four RIS states. Paper [26] reported that the use of 2-bit phase shifters is practically sufficient to achieve close to optimal performance. Paper [27] mentioned that a 3-bit resolution yields a very close result to the one obtained for ideal phase shifts. And work [28] demonstrates that the 4-bit resolution can deliver desirable results. Here, from our results, it can be observed that for 1-bit resolution, the scattering losses are quite high for all four RIS states, while the 4-bit resolution leads to very similar results as for the continuous loads. For the sake of spectral and cost efficiency, two-bit quantization resolution can be employed as a trade-off since the power loss from the two-bit resolution is quite low.

III. RAY TRACING SIMULATIONS

The results in Sec. II are based on the free-space path loss model, with only one LOS path between the TX and RIS, and one LOS path between the RIS and RX. To analyze wave propagation in more realistic environments, ray tracing is a very useful method since it accounts for the effect of the environment. There are several ray tracers already in academic and commercial use, such as the *MATLAB* ray tracer, the *Wireless InSite* from Remcom [29], the *CloudRT* from Beijing Jiaotong University [30], and more. So far, only the *Wireless InSite* ray tracer supports RISs in its engineered electromagnetic surfaces (EES) module, but it is in an idealized fashion and users cannot easily reconfigure the EES module for different RISs. Therefore, we aim to find a way that can flexibly implement different types of RISs into a ray tracer. To simulate a RIS-assisted scenario in a ray tracer, we have to first model a RIS into it. In this section, we first incorporate our designed RIS model in the *MATLAB* ray tracer and verify the simulated results against the theory in Sec. III-A. After that, we extend the simulation scenario from a simple single-input single-output (SISO) case to a multi-user scenario with only LOS paths in Sec. III-B and the same scenario with multi-path propagation in Sec. III-C to analyze the ray tracing simulation results.

A. Verification in a SISO Scenario

Since the RIS-tailored *Vienna SLS* supports the *MATLAB* ray tracer [10], [11], we utilize the *MATLAB* ray tracer to

accommodate RIS functionality by modeling the RIS as two separate antennas with imported E-field data from *CST*. For each RIS size at each propagation mode, we have two RIS patterns, one towards the incidence direction and the other toward the realized anomalous reflection angle. Therefore, in the ray tracer, we first simulate the TX-RIS link where the RIS is used as a receiver. Next, we simulate the RIS-RX link where the RIS is used as a transmitter [31], [32]. From ray tracing simulations, we obtain the received power at the RIS from the TX-RIS link. This power is then used as the transmitted power for the RIS-RX link simulations. Similarly, we obtain the received power at the RX antenna. In this model, we assume that the RIS is a fully passive reflector that reflects all the power that it receives and does not consume any power by itself.

To validate the RIS implementation in the ray tracer by the theory, we set up the same SISO scenario in the ray tracer as in Sec. II. The scenario setup parameters are summarized in Table III. When the RIS is used as a receiver for the TX-RIS link, the RIS pattern is toward 0° , facing the TX antenna. When the RIS is used as a transmitter for the RIS-RX link, the reflection pattern of the RIS is towards 13° , 27° , 43° , and 65° for RIS states 1, 2, 3, 4, respectively. The TX and RX direct link is blocked by a wall so that there is no LOS path between them. First, the reflection path number is set as 0, so that we only observe the LOS paths TX-RIS and RIS-RX. All walls, ceilings, and floors in this scenario are considered perfect absorbers to provide a direct point of comparison with the LOS path loss models considered above.

TABLE III
SETUP PARAMETERS FOR THE SISO SCENARIO

Parameter	Value
Center frequency	26 GHz
TX antenna	omnidirectional (0 dB gain)
RX antenna	omnidirectional (0 dB gain)
Transmit power at the TX antenna	10 dBW
Distance between the TX and RIS	17.00 m
Distance between the RIS and RX	17.22 m

The comparison results between the ray tracing simulation and method 1 from Sec. II-A are plotted in Fig. 4. Figures 4(a), 4(b), 4(c), and 4(d) show results for RIS states 1, 2, 3, 4, respectively. From the four figures we can observe that the ray tracing simulation results are very close to the theoretical results that we have obtained for method 1. The larger the RIS size, the larger the differences between the two results for all four RIS states. However, even the largest difference that appears for RIS state 4 is about 0.6 dB. The comparison results indicate that our strategy of modeling RIS in the ray tracer seems correct for the LOS link.

B. Multi-user Scenario with only LOS Paths

In this section, we extend the simulation to a multi-user scenario, as shown in Fig. 5. The room size is $24 \times 25 \times 3$ (m^3) in terms of width \times length \times height. There is one 1×1 m^2 glass window on the southern wall, and a 1.3×2.5 m^2 door on the northern wall. In the southwest corner of the room, there is a small cabinet with a height of 2 m. The material of the whole indoor room is set as “concrete” since the *MATLAB* ray tracer up to version 2024a does not support multiple materials

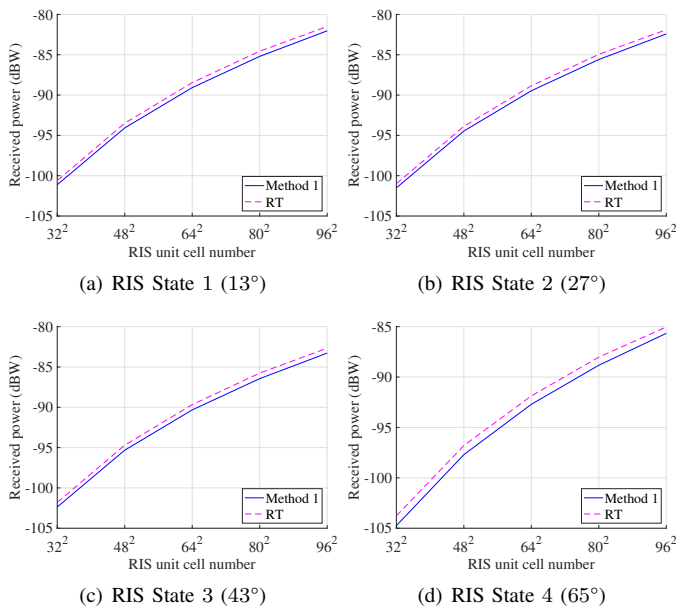


Fig. 4. Results comparison between Method 1 and ray tracing (RT) for the four different RIS states.

for an imported 3D object. The direct link between the TX and RX antennas is blocked by two inner walls in the room. The TX antenna is a horn antenna with the maximum gain of 18.5 dBi toward 0° from the RIS. To investigate how the RX antenna location influences the received power, we place 450 test omnidirectional RX antennas at different locations in the room, shown as blue icons. The spacing between the adjacent RX antennas is 0.6 m.

The RISs for state 1 to state 4 with five different sizes are placed at the same location in the room with their receiving beams toward the TX antenna. The far-field distances of the five RIS sizes are 1.80, 4.04, 7.19, 11.23, and 16.17 m for the sizes of $32 \times 32 A_0$, $48 \times 48 A_0$, $64 \times 64 A_0$, $80 \times 80 A_0$, and $96 \times 96 A_0$, respectively, according to the calculation $R = 2D^2/\lambda$ with D the largest dimension of the antenna. Hence, the distance between the TX and the RIS is set to 22 m, and the distance between the RIS and the RX antenna is from 17.4 m to 22.8 m to fulfill the far-field assumption. The RX antennas are placed at 10 arcs with the RIS location being the center point of the arcs. The angle range of the RX antennas toward the RIS is from 10° to 85.4° from northwest to southeast in the room. The height of TX, RX, and the RIS is 1.5 m.

To investigate whether the RX antennas at different locations benefit from the RIS, we simulate the LOS path from the TX to the RIS and from the RIS to each RX antenna for all four RIS states. Then we take the maximum received power for each RX antenna among all four RIS states. In this way, the RX antennas located at 13° , 27° , 43° , and 65° should all receive strong power due to the RIS assistance. The received power for all the users at different angles and distances from the RIS is plotted in Fig. 6. Figures 6(a), 6(b), 6(c), 6(d), and 6(e) display the results for the $32 \times 32 A_0$, $48 \times 48 A_0$, $64 \times 64 A_0$, $80 \times 80 A_0$, and $96 \times 96 A_0$ RIS sizes, respectively. The radius of the polar plot is the distance between the RX and the RIS. The RIS is located at point 0 in these figures. The

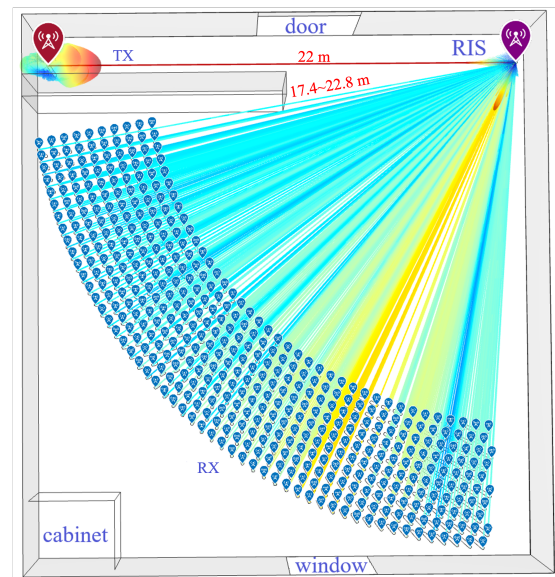


Fig. 5. An indoor scenario with RIS in the *MATLAB* ray tracer.

color of these figures' curves represents the received power.

From Fig. 6 we can observe that the RXs located at 13° , 27° , 43° , and 65° receive the highest power. The RXs at other angles receive lower power because there is no strong reflection from the RIS in those angle ranges. With an increased distance between the RIS and the RX antenna, the received power is slightly reduced. However, since the distance change is not so much from 17.4 m to 22.8 m, the power reduction is not so significant. The maximum received power at the RXs increases from -92.4 dB to -74.5 dB with the RIS size increasing from $32 \times 32 A_0$ to $96 \times 96 A_0$.

To have a more detailed look at the received power at different angles from a RIS, we plot the received power versus the angle with only a $48 \times 48 A_0$ -sized RIS in Fig. 7. Figures 7(a) to 7(d) show the results for RIS State 1 to RIS State 4, respectively. At each angle, there are multiple points representing multiple RX antennas at that angle with different distances from the RIS. It is obvious that the received powers at the four main reflection directions are the highest, while the powers at other angles are lower since the RIS does not cover those angles.

Next, we choose 39 RX antennas that are on the first arc at the 17.4 m distance from the RIS. The received powers at the RX antennas for five RIS sizes are plotted in Fig. 8(a). The calculated differences of received powers at different RIS reflection angles are consistent with the results for the SISO scenario in Sec. III-A. When the angle toward the RX antenna is not at one of the RIS reflection angles, the received power of these RX antennas is much lower. The differences between the five RIS sizes at those angles are also not very significant. The empirical cumulative distribution function (ECDF) results are plotted in Fig. 8(b) to compare the overall received power at all the RX antennas for the five RIS sizes.

C. Multi-user Scenario with Multi-path Propagation

In this section, we consider a multi-path propagation scenario. The setup is the same as in Sec. III-B, except that in this scenario we include reflection paths. It should be noted that

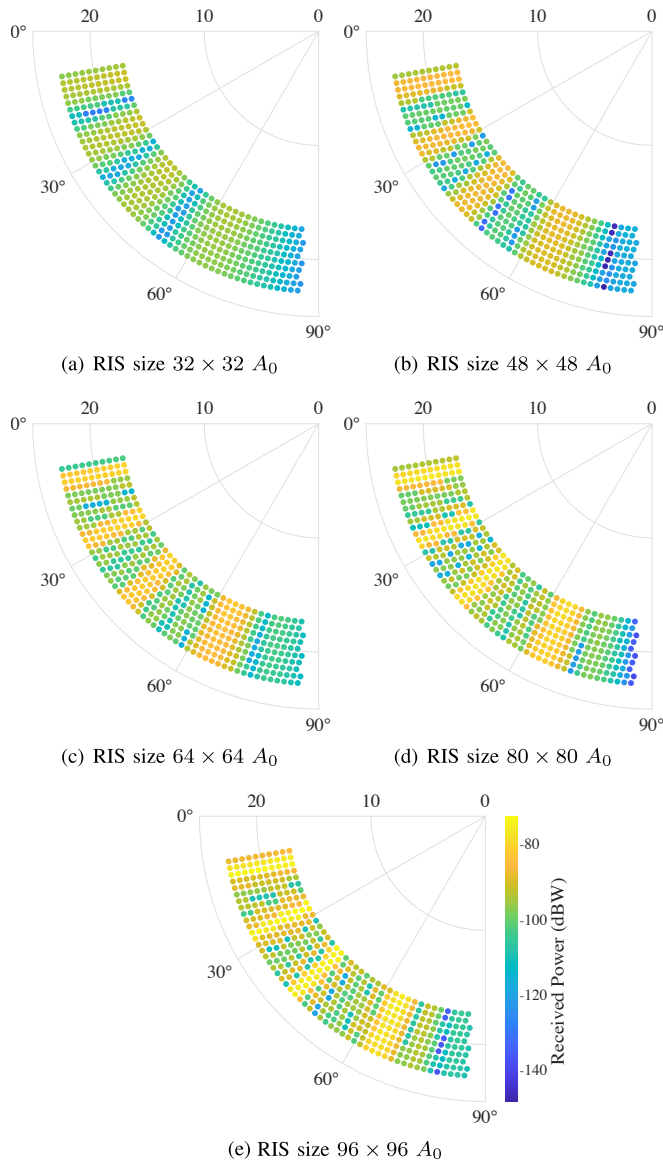


Fig. 6. Received power vs. the angles and distances between the RXs and RIS for different RIS sizes without reflections.

since our RIS is designed for illumination at normal incidence and reflections into a set of four angles, it can be effectively used only for these paths and for the reciprocal ones. The RIS scattering patterns for illuminations from other directions need to be calculated separately (for RIS realized as periodical arrays, this issue is considered in [21]). For simplicity, here we consider only one LOS path for the TX-RIS link, but three reflection paths for the RIS-RX link. To investigate the difference of the received power at the RIS between the LOS path and reflection paths, we run simulations with 0, 3, and 6 reflections, and find that the difference between the LOS and 3 or 6-reflections paths is smaller than 1 dB, which is very small. Hence, even though it is not so realistic to assume only one LOS path between the TX and the RIS, it is still reasonable to use this assumption for simulations.

The received power results versus the distances to the RX antenna and the angles are shown in Fig. 9. In addition to the results with five RIS sizes that are shown in Figs. 9(b) – 9(f), the results without RIS are plotted in Fig. 9(a). From these

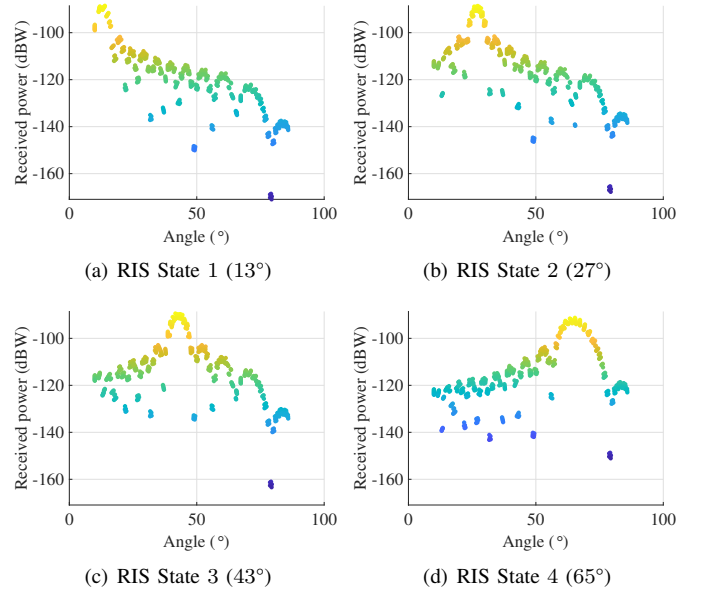


Fig. 7. Received power vs. the angles between the users and the RIS for $48 \times 48 A_0$ -sized RIS without reflections.

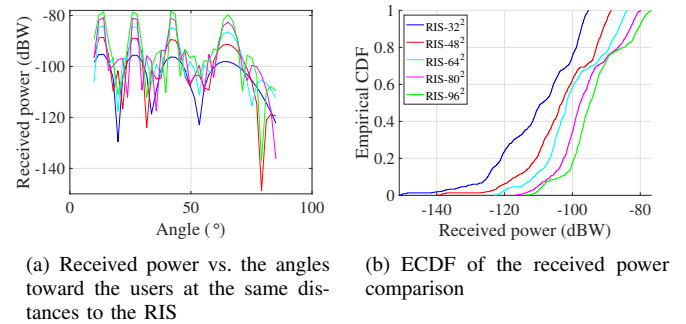


Fig. 8. Received power comparison for different RIS sizes without reflections. (The two subfigures use the same legend in (b).)

figures, we notice that when there is no RIS, only some RX antennas located in the range of $[10^\circ \ 41^\circ]$ receive relatively high power, while many RX antennas receive only noise. However, when including a RIS in this scenario, almost all RX antennas are covered and receive a significant amount of signal power. Especially when the RIS size gets larger, the received powers at the users become higher.

The received power as a function of the angle for the $48 \times 48 A_0$ -sized RIS is plotted in Fig. 10. In addition to the results for RIS states 1 to 4, as shown in Fig. 10(b) to Fig. 10(e), we also plot the results without RIS in Fig. 10(a). In the scenario without RIS, most users in the range of $[10^\circ \ 50^\circ]$ receive more than -110 dB power, which is mainly due to reflections from the room walls. Since the users in the $[10^\circ \ 41^\circ]$ range already receive strong powers from reflection paths, the impact of a RIS with the states 1 and 2 (13° and 27°) is not so obvious, as is seen in Figs. 10(b)-10(c). However, since the users beyond that range are not covered by reflected waves, the improvement due to the RIS is quite significant at states 3 and 4 (43° and 65°), as shown in Figs. 10(d)-10(e). In addition, compared to the LOS scenario in Fig. 7, the received powers at the users are mostly improved in the multipath scenario. For example, in the LOS scenario, many users

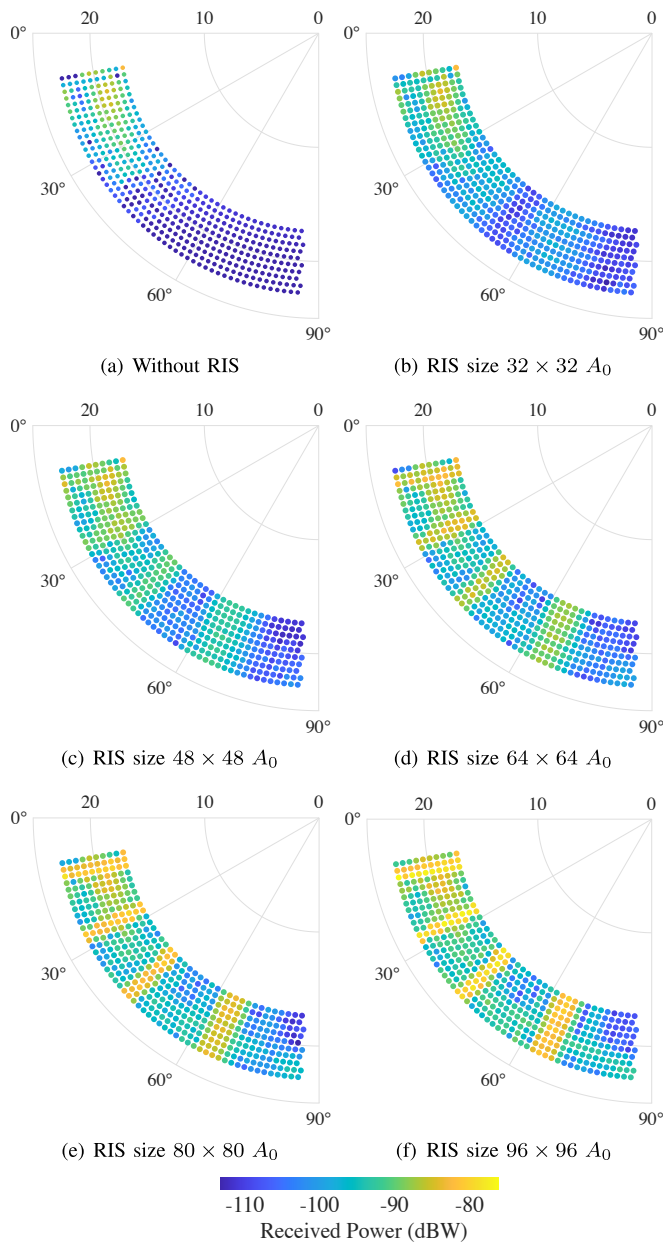


Fig. 9. Received power vs. angles and distances between the users and the RIS of different sizes with 3 reflections.

receive power between $[-140 -120]$ dBW. However, in the multi-path scenario, the majority of users receive higher than -120 dBW. It is obvious that after multiple reflections from the walls, floor, ceiling, and cabinet, the transmitted signals have a good chance of reaching those RX antennas in blind spots.

Similarly, in Fig. 11(a) we compare the results for RISs of five sizes with 39 RX antennas at the first arc that is 17.4 m away from the RIS. Compared to the case without RIS, the scenarios with RIS lead to significant improvement of received power at these RXs, especially at the RIS reflection directions and with a larger RIS size. The ECDF results of the received power are plotted in Fig. 11(b).

In summary, the strategy of implementing a RIS as an antenna in a ray tracer is proved to be correct, which can also be applied to other ray tracers. The ray tracing simulation

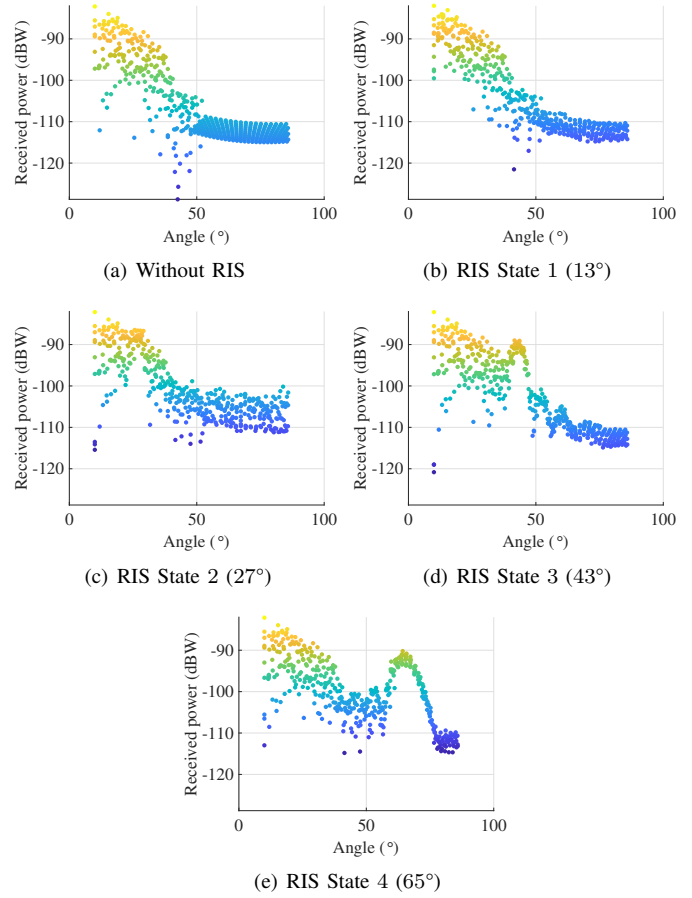
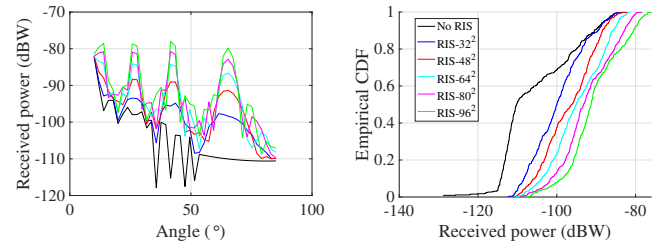


Fig. 10. Received power vs. the angles between the users and the RIS for $48 \times 48 A_0$ -sized RIS with 3 reflections.



(a) Received power vs. angles of the users which have the same distances to the RIS (b) ECDF of the received power comparison

Fig. 11. Received power comparison with different RIS sizes with 3 reflections. (The two subfigures use the same legend in (b).)

results from a SISO and multi-user LOS scenario prove that the maximum received powers at the RX antennas fulfil the power scaling law [25], which is actually from the communication theory where it just considers the RIS element number and phase shifts and does not involve any EM properties of the RIS, but our RIS model is from EM perspective and modeled as a whole antenna. So far we have reached a good agreement when applying the communication theory to a realistic RIS from the EM perspective. In addition to the comparison between the scenario with multiple reflections and without reflections, we can conclude that the contributions of a RIS are highly dependent on its reflection directions, the RIS sizes, and the reflections from the environment. The user

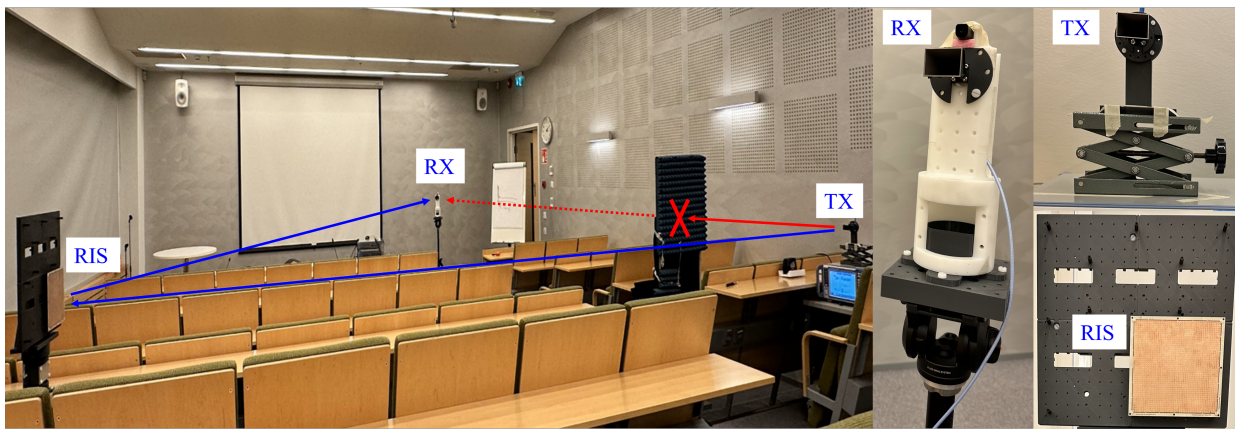
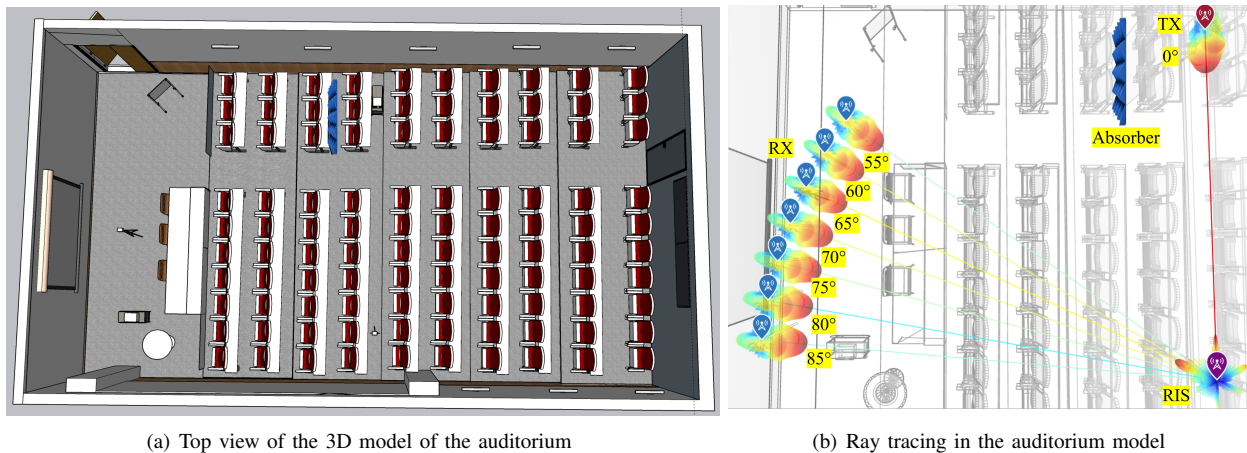


Fig. 12. Measurement setup in the auditorium with the 48×48 -sized static AR prototype, TX, and RX antennas.



(a) Top view of the 3D model of the auditorium

(b) Ray tracing in the auditorium model

Fig. 13. Ray tracing model of the auditorium.

located at the RIS reflection angles can receive the maximum power, the bigger RIS size also contributes more power to the user, and reflection paths in the environment can contribute to the user coverage improvement.

IV. EXPERIMENTAL RESULTS

In Part I we introduced a prototype of a static 48×48 array with the dimension of $152.6 \text{ mm} \times 152.6 \text{ mm}$ and measured the scattering pattern of it in an anechoic chamber which can be seen in Fig. 9 in Part I. Different from the perfectly functioning RIS we used in the previous sections, the prototype utilizes lossy material and 3-bit quantization that achieves eight different phase shifts. In this part, we performed over-the-air measurements at 26 GHz with the same prototype in an auditorium at Nokia Bell Labs Espoo office to test the communication link performance and our ray tracing model with the realistic AR.

A. Indoor Measurement and Ray Tracing Settings

The measurement scenario is shown in Fig. 12. The parameters of the measurement setup are listed in Table IV. The TX horn antenna is connected to a vector signal generator via a cable, the RX horn antenna is connected to a low noise amplifier (LNA), and then connected to a signal & spectrum analyzer via cables. The signal generator is connected to the

TABLE IV
PARAMETERS OF THE MEASUREMENT SETUP

Parameters	Value
Frequency	26 GHz
Dimension of the auditorium	$14 \times 8 \times 3 \text{ (m}^3\text{)}$
Height of TX, RX, and RIS	1.5 m
Distance between TX and RIS	$R_1 = 5.5 \text{ m}$
Distance between RX and RIS	$R_2 = 7 \text{ m}$
TX horn antenna	max. gain of 18 dBi
RX horn antenna	max. gain of 18 dBi
Beam width of TX/RX antenna	22° at 26 GHz
Transmitted power at the TX antenna	$P_t = 6 \text{ dBm}$
TX cable loss	$L_t = 2.5 \text{ dB}$
RX cable loss + LNA gain	$G_a = 19.9 \text{ dB}$

signal & spectrum analyzer through a reference clock and Ethernet cable for synchronizing the signals. We use a 400-MHz channel bandwidth and 16 quadrature amplitude modulation (QAM) modulated 5G NR wave mode for transmitted signals.

To measure the TX-AR-RX link, we use a wave absorber to block the direct link between the TX and the RX antennas. The TX and the AR are fixed and are facing each other. The RX antenna is placed at $55^\circ, 60^\circ, \dots, 85^\circ$ of the AR, respectively, but the distance between each RX location and the AR is always 7 m. We orient the direction of the RX antenna to

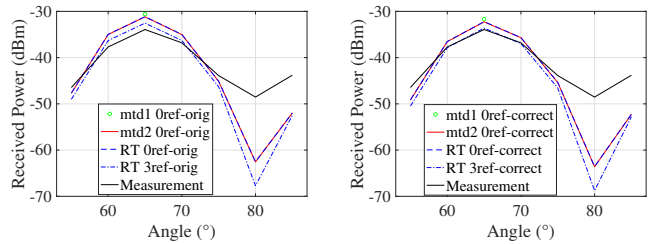
always face the AR at each location. In the end, we obtain 7 different received power values at the RX antenna from the 7 different locations. We denote this power as P_m in dBm.

To simulate the same measurement scenario in a ray tracer, we first create a 3D model using *SketchUp* and import it to the *MATLAB* ray tracer. The top view of the model is displayed in Fig. 13(a). This 3D model replicates the real dimensions of the whole room and the objects inside it. We model a horn antenna in *MATLAB* and use it for TX and RX antennas in ray tracing simulations. The maximum gain of the horn antenna is 18 dBi. Then we use the same way as in Sec. III to implement the realistic AR in the *MATLAB* ray tracer. The locations of the TX, RX antennas, and the AR are the same as in the measurement. Figure 13(b) shows the ray tracing of the TX-AR LOS link and the AR-RXs LOS links. We first set the reflection number as 0 to observe the received power from the AR-assisted LOS links, and compare it with the theoretical results obtained from Sec. II, since the two methods in Sec. II also considers only the LOS paths. Then, we set 3 reflections in ray tracing simulations to include the reflection paths from the room objects and compare the results with measurement results, since the reflections cannot be ignored in a realistic environment. We denote the simulated powers at 7 locations as $P_{r,orig}$. Then, considering the cable losses and the LNA gain, we obtain $P_{RT,orig} = P_{r,orig} - L_t + G_a$.

B. Results Comparison between the Theoretical Model, Ray Tracing, and Measurement

In this section, we first compare the received power results between the two methods from Sec. II, the measurement result P_m , and the ray tracing simulation result $P_{RT,orig}$ as shown in Fig. 14(a). It is worth noting that method 1 can only give the results at the RIS targeted direction, it cannot be used to calculate received powers at other directions that the RIS is not designed for. In our case, we only consider the received power at 65° with method 1 since this AR is designed for 65° . We denote this result as $P_{mtd1,orig}$. With method 2 and ray tracing, we obtain received powers also at other angles by utilizing the respective RIS radiation patterns from *CST* simulations. The result from method 2 is denoted as $P_{mtd2,orig}$. From Fig. 14(a) we observe that the ray tracing results with zero reflection are the same as from method 2, and they are very close to the theoretical result from method 1, which is consistent with our analysis in Sec. II-C and Sec. III-A. However, the ray tracing results with 3 reflections have about 1.4 dB difference compared to measurement results at 60° and 65° .

To investigate whether this difference is from our ray tracing model or from the measurement system, we perform a reference measurement for the TX-RX link and compare it with theoretical results. In this reference measurement, we do not include the AR and the absorber, but let the TX and RX antennas directly face each other every time when we move the RX antenna to the 7 locations. The results from this measurement are denoted as $P_{m,LOS}$ in dBm. Because it is very easy to validate this kind of LOS scenario through theory, i.e., we calculate the received power at the Rx antenna through free space path loss from the TX using



(a) Original results from analytical Methods 1 and 2, ray tracing simulations with 0 and 3 reflections, and from measurements (b) Power-corrected results from the analytical Methods 1 and 2, ray tracing simulations with 0 and 3 reflections, and from measurement.

Fig. 14. Original and corrected power obtained from two analytical methods, ray tracing simulations and measurements. (“mtd1” and “mtd2” are abbreviations of “Method 1” and “Method 2”, “RT” means ray tracing simulation, “0ref” and “3ref” means 0 reflection and 3 reflections, respectively.)

the equation $P_{FS} = P_t G_t G_r \left(\frac{\lambda}{4\pi R}\right)^2$ in W, where R is the distance between the TX and RX antennas. Then adding the cable losses and LNA gain, we obtain a theoretical received power $P_{theory} = P_{FS} - L_t + G_a$ in dBW, where the P_{FS} here is in dBW. We find the power differences between the theoretical value and the measurement results are very small: $P_{diff} = P_{theory} - P_{m,LOS} = [1.5, 1.6, 1.1, 0.7, 0.3, 1.0, 0.3]$ dB for the angles of $[55^\circ, 60^\circ, 65^\circ, 70^\circ, 75^\circ, 80^\circ, 85^\circ]$, respectively. This difference may be due to the system loss in our measurement setups, including alignment errors of the antennas, and is not included in the theoretical model.

Now if we take into account the P_{diff} when comparing the simulations and measurement results, i.e., use this P_{diff} to correct the theoretical and simulation results and obtain $P_{mtd1,correct} = P_{mtd1,orig} - P_{diff}$, $P_{mtd2,correct} = P_{mtd2,orig} - P_{diff}$, and $P_{RT,correct} = P_{RT,orig} - P_{diff}$. The comparison with measurement results P_m is shown in Fig. 14(b). We find the measurement results at 60° , 65° , and 70° now agree very well with the ray tracing results with 3 reflections. We can thus conclude that our designed RIS works as we expected. It is also proved that our theoretical analysis for a RIS-assisted link is correct, the 3D auditorium model is accurate, the RIS implementation in the *MATLAB* ray tracer is correct, the theoretical analysis and ray tracing methods work not only for a perfect RIS but also for a realistic lossy AR.

V. CONCLUSION AND OUTLOOK

In Part I we studied the scattering synthesis for multimode ARs and developed an efficient mmWave AR to be used in this work. In Part II, we used the designed perfect RIS and the manufactured reflector prototype to evaluate their EM properties and communication performances. We implemented both the RIS and the AR into the *MATLAB* ray tracer and validated the results with the theory. In addition, we investigated the quantization effect on the RIS implementation. Furthermore, we analyzed the large-scale fading of RIS-assisted communication links through EM simulation, system-level, and ray tracing simulations, as well as through indoor measurements in a room using a static AR as a test vehicle. The results demonstrated that our RIS design from the EM aspects, RIS implementation in the ray tracer, and the system-level and ray tracing simulations with the two RISs from the communication

aspects, are all correct and consistent with the measurement results.

From the EM design perspective, we acknowledge that our designed multi-mode reflector is intended for reflection in discrete anomalous angles. The coverage between these angles is a topic of an extension to this work in the future. The unit cell loads of the multi-mode reflector would be made reconfigurable so that a non-perfect anomalous reflection in the gap angles would be allowed by the design, however improving the coverage between the discrete modal anomalous angles. Another possibility is to construct a multi-mode static anomalous reflector from multiple single-reflection angle sub-panels, i.e., not having a RIS as a reconfigurable surface, but multiple static anomalous reflectors side-by-side to implement the same functionality as the multi-mode RIS would do.

From the communication perspective, we admit that this work only reported a simple measurement and evaluated simple results. However, more measurement results and communication performance analysis with the AR prototype will be reported in our following work. This work has validated the connections between the EM and communication analysis for a RIS, which can accelerate the RIS technology realization. For example, by passing a limited set of macroscopic RIS parameters from the EM design to the RIS-tailored Vienna system-level simulator and a ray tracer, one can simulate the RISs in realistic large-scale scenarios, taking the propagation environment's effects into consideration. This work also provides an analytical framework for the RIS analysis such that others can use our strategies to analyze and validate their developed RISs/ARs/reflectarrays, as long as the radiation patterns or geometrical area and the incidence and reflection angles are available. By using the simulation software with our RIS implementation method, one can predict the system performance accurately in the presence of RISs/ARs/reflectarrays in realistic environments, potentially reducing measurement costs.

ACKNOWLEDGEMENT

The authors express gratitude to Professor Do-Hoon Kwon from the University of Massachusetts Amherst, USA, for the valuable suggestions and discussions regarding array antenna scattering synthesis for periodic reflectors. The authors also acknowledge TU Wien Bibliothek for financial support through its Open Access Funding Program.

REFERENCES

- [1] M. Di Renzo, A. Zappone, M. Debbah, M.-S. Alouini, C. Yuen, J. de Rosny, and S. Tretyakov, "Smart radio environments empowered by reconfigurable intelligent surfaces: How it works, state of research, and the road ahead," *IEEE J. Sel. Areas Commun.*, vol. 38, no. 11, pp. 2450–2525, 2020.
- [2] A. L. Imoize, O. Adedeji, N. Tandiya, and S. Shetty, "6G Enabled Smart Infrastructure for Sustainable Society: Opportunities, Challenges, and Research Roadmap," *Sensors*, vol. 21, no. 5, 2021.
- [3] N. Kim, G. Kim, S. Shim, S. Jang, J. Song, and B. Lee, "Key Technologies for 6G-Enabled Smart Sustainable City," *Electronics*, vol. 13, no. 2, 2024.
- [4] L.-H. Shen, K.-T. Feng, and L. Hanzo, "Five Facets of 6G: Research Challenges and Opportunities," *ACM Comput. Surv.*, vol. 55, no. 11, Feb. 2023.
- [5] W. Tang, M. Z. Chen, X. Chen, J. Y. Dai, Y. Han, M. Di Renzo, Y. Zeng, S. Jin, Q. Cheng, and T. J. Cui, "Wireless communications with reconfigurable intelligent surface: Path loss modeling and experimental measurement," *IEEE Transactions on Wireless Communications*, vol. 20, no. 1, pp. 421–439, 2021.
- [6] W. Tang, X. Chen, M. Z. Chen, J. Y. Dai, Y. Han, M. D. Renzo, S. Jin, Q. Cheng, and T. J. Cui, "Path loss modeling and measurements for reconfigurable intelligent surfaces in the millimeter-wave frequency band," *IEEE Transactions on Communications*, vol. 70, no. 9, pp. 6259–6276, 2022.
- [7] J. Huang, C.-X. Wang, Y. Sun, R. Feng, J. Huang, B. Guo, Z. Zhong, and T. J. Cui, "Reconfigurable intelligent surfaces: Channel characterization and modeling," *Proceedings of the IEEE*, vol. 110, no. 9, pp. 1290–1311, 2022.
- [8] V. Degli-Esposti, E. M. Vitucci, M. D. Renzo, and S. A. Tretyakov, "Reradiation and scattering from a reconfigurable intelligent surface: A general macroscopic model," *IEEE Transactions on Antennas and Propagation*, vol. 70, no. 10, pp. 8691–8706, 2022.
- [9] E. M. Vitucci, M. Fabiani, and V. Degli-Esposti, "Use of a Realistic Ray-Based Model for the Evaluation of Indoor RF Coverage Solutions Using Reconfigurable Intelligent Surfaces," *Electronics*, vol. 12, no. 5, 2023.
- [10] L. Hao, A. Fastenbauer, S. Schwarz, and M. Rupp, "Towards system level simulation of reconfigurable intelligent surfaces," in *2022 International Symposium ELMAR*, 2022, pp. 81–84.
- [11] L. Hao, S. Schwarz, and M. Rupp, "The extended Vienna system-level simulator for reconfigurable intelligent surfaces," in *2023 Joint European Conference on Networks and Communications & 6G Summit (EuCNC/6G Summit)*, 2023, pp. 1–6.
- [12] M. K. Müller, F. Ademaj, T. Dittrich, A. Fastenbauer, B. R. Elbal, A. Nabavi, L. Nagel, S. Schwarz, and M. Rupp, "Flexible multi-node simulation of cellular mobile communications: the Vienna 5G System Level Simulator," *EURASIP Journal on Wireless Communications and Networking*, vol. 2018, no. 1, p. 17, Sep. 2018.
- [13] B. Sihlbom, M. I. Poulakis, and M. D. Renzo, "Reconfigurable intelligent surfaces: Performance assessment through a system-level simulator," *IEEE Wireless Communications*, pp. 1–10, 2022.
- [14] Y. Xing, F. Vook, E. Visotsky, M. Cudak, and A. Ghosh, "Raytracing-Based System Performance of Intelligent Reflecting Surfaces at 28 GHz," in *ICC 2022 - IEEE International Conference on Communications*, 2022, pp. 498–503.
- [15] Z. Li, O. A. Topal, O. T. Demir, E. Björnson, and C. Cavdar, "mmwave coverage extension using reconfigurable intelligent surfaces in indoor dense spaces," in *ICC 2023 - IEEE International Conference on Communications*, 2023, pp. 5805–5810.
- [16] Z. Yun and M. F. Iskander, "Ray tracing for radio propagation modeling: Principles and applications," *IEEE Access*, vol. 3, pp. 1089–1100, 2015.
- [17] Y. L. C. de Jong, "Uniform ray description of physical optics scattering by finite locally periodic metasurfaces," *IEEE Transactions on Antennas and Propagation*, vol. 70, no. 4, pp. 2949–2959, 2022.
- [18] S. K. R. Vuyyuru, R. Valkonen, D.-H. Kwon, and S. A. Tretyakov, "Efficient anomalous reflector design using array antenna scattering synthesis," *IEEE Antennas Wireless Propag. Lett.*, vol. 22, no. 7, pp. 1711–1715, 2023.
- [19] S. K. R. Vuyyuru, R. Valkonen, S. A. Tretyakov, and D.-H. Kwon, "Efficient synthesis of large finite patch arrays for scanning wide-angle anomalous reflectors," *IEEE Open J. Antennas Propag.*, 2024. [Online]. Available: 10.1109/OJAP.2024.3466890
- [20] S. Kosulnikov, F. S. Cuesta, X. Wang, and S. A. Tretyakov, "Simple link-budget estimation formulas for channels including anomalous reflectors," *IEEE Transactions on Antennas and Propagation*, vol. 71, no. 6, pp. 5276–5288, 2023.
- [21] A. Díaz-Rubio and S. A. Tretyakov, "Macroscopic modeling of anomalously reflecting metasurfaces: Angular response and far-field scattering," *IEEE Transactions on Antennas and Propagation*, vol. 69, no. 10, pp. 6560–6571, 2021.
- [22] C. A. Balanis, *Antenna Theory: Analysis and Design*. John Wiley & sons, 2015.
- [23] S. W. Ellingson, "Path loss in reconfigurable intelligent surface-enabled channels," in *2021 IEEE 32nd Annual International Symposium on Personal, Indoor and Mobile Radio Communications (PIMRC)*, 2021, pp. 829–835.
- [24] I. Yildirim, A. Uyrus, and E. Basar, "Modeling and analysis of reconfigurable intelligent surfaces for indoor and outdoor applications in future wireless networks," *IEEE Transactions on Communications*, vol. 69, no. 2, pp. 1290–1301, 2021.

- [25] Q. Wu and R. Zhang, "Intelligent reflecting surface enhanced wireless network via joint active and passive beamforming," *IEEE Transactions on Wireless Communications*, vol. 18, no. 11, pp. 5394–5409, 2019.
- [26] Q. Wu, S. Zhang, B. Zheng, C. You, and R. Zhang, "Intelligent reflecting surface-aided wireless communications: A tutorial," *IEEE Transactions on Communications*, vol. 69, no. 5, pp. 3313–3351, 2021.
- [27] M. Najafi, V. Jamali, R. Schober, and H. V. Poor, "Physics-based modeling and scalable optimization of large intelligent reflecting surfaces," *IEEE Transactions on Communications*, vol. 69, no. 4, pp. 2673–2691, 2021.
- [28] S. F. Zamanian and S. M. Razavizadeh, "3D beamforming in Intelligent Reflecting Surface (IRS)-assisted multi-user cognitive radio networks," *Physical Communication*, vol. 56, p. 101951, 2023.
- [29] L. Gotszald, "Novel Tracing Algorithm vs Remcom Wireless InSite," *International Journal of Electronics and Telecommunications*, vol. 61, no. No 3, 2015.
- [30] K. Guan, D. He, and Z. Zhong, "CloudRT: A Chinese example of open science infrastructure and services," *Cultures of Science*, vol. 4, no. 4, pp. 217–226, 2021.
- [31] L. Hao, F. S. Cuesta, S. A. Tretyakov, and M. Rupp, "Improving propagation channels with static scatterers," *IEEE Antennas and Wireless Propagation Letters*, pp. 1–5, 2024.
- [32] L. Hao, F. S. Cuesta, S. A. Tretyakov, and M. Rupp, "Optimizing propagation channels using static scatterers: Modeling and ray-tracing simulations," in *2024 IEEE International Symposium on Antennas and Propagation and INC/USNC-URSI Radio Science Meeting (AP-S/INC-USNC-URSI)*, 2024, pp. 37–38.



Le Hao (Member, IEEE) received a B.Eng. degree in Electronics Science and Technology and an M.Eng. degree in Control Science and Engineering from Tongji University, China, in 2017 and 2020, respectively. She received a Dr. Techn. degree in Telecommunications from Technische Universität Wien (TU Wien), Austria, in 2024. She is currently a postdoctoral researcher at the Institute of Telecommunications at TU Wien. Her research interests include reconfigurable intelligent surfaces (RIS), ray tracing, signal processing, and reinforcement learning in mobile communication systems.

ing in mobile communication systems.



Markus Rupp (Fellow, IEEE) received the Dipl.Ing. degree from the University of Saarbrücken, Germany, in 1988, and the Dr.Ing. degree from Technische Universität Darmstadt, Germany, in 1993. Until 1995, he held a postdoctoral research position with the University of California at Santa Barbara, Santa Barbara, CA, USA. From 1995 to 2001, he was with the Nokia Bell Laboratories, Wireless Technology Research Department, Holmdel, NJ, USA. Since 2001, he has been a Full Professor in digital signal processing in mobile communications

with TU Wien.



Sravan Kumar Reddy Vuyyuru (Member, IEEE) received a B.Tech degree from the Hindustan Institute of Technology & Science (HITS), Chennai, India, in 2018 and a joint diploma M.S. degree from the Erasmus Mundus Innovative Microwave Electronics and Optics (EMIMEO) master program in the University of Limoges, Limoges, France, and the University of Brescia, Brescia, Italy, in 2021. He is currently a Marie Skłodowska Curie fellow with the MetaWireless project working at Nokia Bell Labs, Oulu, Finland, and pursuing a Ph.D. degree

under the supervision of Prof. Sergei A. Tretyakov with the Department of Electronics and Nanoengineering, School of Electrical Engineering, Aalto University, Espoo, Finland. His research interests include applied electromagnetics, antennas, ray tracing, and reconfigurable intelligent surfaces for anomalous reflection and sensing for wireless integrated sensing and communications, especially in the mmWave range.



Sergei A. Tretyakov (Fellow, IEEE) received the Dipl. Engineer-Physicist, Ph.D., and D.Sc. degrees in radiophysics from Saint Petersburg State Technical University, Saint Petersburg, Russia, in 1980, 1987, and 1995, respectively.

From 1980 to 2000, he was with the Radiophysics Department, Saint Petersburg State Technical University. He is currently a Professor of radio science with the Department of Electronics and Nanoengineering, Aalto University, Espoo, Finland. He has authored or coauthored six research monographs

and more than 370 journal articles. His current research interests include electromagnetic field theory, complex media electromagnetics, metamaterials, and microwave engineering.

Dr. Tretyakov served as the General Chair of the International Congress Series on Advanced Electromagnetic Materials in Microwaves and Optics (Metamaterials) from 2007 to 2013. He served as the President of the Virtual Institute for Artificial Electromagnetic Materials and Metamaterials (Metamorphose VI). He served as the Chairperson of the St. Petersburg IEEE Electron Devices (ED)/Microwave Theory and Techniques (MTT)/Antennas & Propagation (AP) Chapter from 1995 to 1998.



Risto Valkonen (Member, IEEE) received the M.Sc. (Tech.) degree in communications engineering and the D.Sc. (Tech.) degree in electrical engineering from Aalto University, Finland, in 2007 and 2013, respectively. From 2006 to 2013, he was with the Department of Radio Science and Engineering, Aalto University. From 2013 to 2015, he was Postdoctoral Researcher with the University of Kiel. Since 2015, he has been with Nokia and since 2016 with Nokia Bell Labs as Antenna Specialist. His research interest includes antennas and RF front-

ends for future communication systems.



Artan Salihu (Graduate Student Member, IEEE) received his M.Sc. degree from the University of Pittsburgh, Pittsburgh, PA, USA, in 2016, and his Dr. techn. degree from TU Wien, Austria, in 2024. His research interests include deep learning and wireless localization.